Kashaev, N.; Ventzke, V.; Horstmann, M.; Riekehr, S.; Yashin, G.;
Stutz, L.; Beck, W.:

Microstructure and Mechanical Properties of Laser Beam Welded Joints between Fine-Grained and Standard Ti-6Al-4V Sheets Subjected to Superplastic Forming

In: Advanced Engineering Materials (2014) Wiley

DOI: 10.1002/adem.201400202

Microstructure and Mechanical Properties of Laser Beam Welded Joints between Fine-Grained and Standard Ti-6Al-4V Sheets Subjected to Superplastic Forming

Nikolai Kashaev[1], Volker Ventzke[1], Manfred Horstmann[1], Stefan Riekehr[1], Grigory Yashin[1], Lennart Stutz[2], and Werner Beck[2]

[1]*Helmholtz-Zentrum Geesthacht, Institute of Materials Research, Materials Mechanics / ACE-Centre, Max-Planck-Straße 1, 21502 Geesthacht, Germany*

[2]*FormTech GmbH, Mittelwendung 26, 28844 Weyhe, Germany*

Corresponding Author: Dr. Nikolai Kashaev
Phone: +49 4152 87-2536
Fax: +49 4152 87-42536
E-mail: nikolai.kashaev@hzg.de

Abstract: A fine-grained Ti-6Al-4V sheet that has been developed for superplastic forming was joined to a standard Ti-6Al-4V sheet using a Nd:YAG laser and alloy compatible filler wire. The microstructural and mechanical properties of dissimilar laser beam welded butt joints were investigated to determine their behaviour under static and cyclic loads and for superplastic forming. The filler wire affected the heat input and reduced the increase in the hardness within the fusion zone compared to that in the heat-affected zone. Moreover, the laser beam welding process activated local microstructure transformations that were associated with local changes in the microtexture, the β content and the grain size. The mechanical behaviour of a dissimilar laser beam welded butt joint under a static tensile load was controlled by the properties of the standard Ti-6Al-4V sheet. It is well known that geometrical notches affect fatigue behaviour, and fatigue fracture usually occurs within the heat-affected zones adjacent to the welding seam. However, removing the geometrical notches did not significantly improve the fatigue behaviour because local microstructural and microtextural changes still created metallurgical notches. Superplastic forming was observed in the fine-grained Ti-6Al-4V sheet without crack formation in the heat-affected zones or the fusion zone. The welding seam of the dissimilar fine-grained-standard butt joint was resistant to superplastic forming.

Keywords: *titanium alloy, fine-grained Ti-6Al-4V, laser beam welding, microstructure, mechanical properties, superplastic forming*

1. Introduction

Ti-6Al-4V alloys are well known for their high strength, low density, sufficient ductility and outstanding corrosion resistance (Peters et al., 2002). Therefore, these alloys have been widely used in the production of aerospace components and structures as well as medical and surgical devices. Furthermore, metallic components are increasingly made from Ti-6Al-4V alloys to integrate carbon fibre reinforced polymer structures (CFRP) (Murakami et al., 2011; TITAL, 2013). CFRP-Ti structures have found application in airplanes such as Airbus A350 and Boeing B787 (Hombergsmeier, 2010; Murakami et al., 2011; Petersen, 2012; Hanse-

Aerospace e.V., 2012). The successful fabrication of Ti-6Al-4V lightweight structures requires efficient joining technologies and the availability of data on the mechanical and microstructural properties of welded titanium structures. In recent years, a variety of welding processes for Ti-6Al-4V have been developed, such as gas tungsten arc welding (GTAW) (Balasubramanian et al., 2011; Balasubramanian et al., 2011; Oh et al., 2003), electron beam welding (EBW) (Balasubramanian et al., 2011; Balasubramanian et al., 2011; Oh et al., 2003; Li et al., 2011; Saresh et al., 2007; Wang and Wu, 2012, Wanjara et al. 2005), laser beam welding (LBW) (Balasubramanian et al., 2011; Balasubramanian et al., 2011; Cao and Jahazi, 2009; Torster et al., 1999; Pei-quan, 2012; Squillace et al., 2012; Tsay and Tsay, 1997; Wang et al. 2003; Jianxun et al., 2012; Rai et al., 2007) and hybrid joining processes, e.g., laser gas metal arc welding (Petersen, 2012). From an industrial perspective, the LBW technique can be used to realise high working speeds and is the most cost-efficient and easy controllable joining process for the production of Ti-6Al-4V parts (Rosell, 2013; Vallhagen, 2013). LBW allows the welding of complex geometric shapes that are optimised in terms of mechanical stiffness, strength, production velocity and visual quality. The essential criterion for the industrial application of laser beam welded Ti-6Al-4V structures is the availability of reliable data with which to assess damage tolerance behaviour. Laser beam welded Ti-6Al-4V joints exhibit a balanced microstructure and high tensile strength (Squillace et al., 2012; Cao and Jahazi, 2009; Torster et al., 1999; Pei-quan, 2012; Wang et al., 2003). However, little research has been conducted on how the microstructure of laser beam welded Ti-6Al-4V joints affects their fatigue behaviour (Balasubramanian et al., 2011; Balasubramanian et al., 2011; Squillace et al., 2012; Tsay and Tsay, 1997).

Novel fine-grained Ti-6Al-4V sheets (denoted as FG) have recently become available (Salishchev, 2004). Ti-6Al-4V sheets that exhibit a fine-grained microstructure are characterised by high strength and reduced process temperatures and times in the superplastic forming (SPF) process (Beck, 2002). Therefore, cost-effective industrial manufacturing processes can be realised in conjunction with enhanced environmental performance (Salishchev, 2004). However, this new material has not been approved for aerospace applications, and Ti-6Al-4V FG sheets are more expensive than standard Ti-6Al-4V sheets (denoted as STD). Thus, the superior properties of Ti-6Al-4V FG sheets may be dissimilarly combined with Ti-6Al-4V STD sheets to enhance the functionality and reduce the cost. Both materials were produced by the VSMPO-AVISMA company (VSMPO Avisma, 2013).

In this study, dissimilar LBW was performed using Ti-6Al-4V FG sheets and aircraft-approved Ti-6Al-4V STD sheets. The laser beam welded FG-STD butt joint was studied in terms of its tensile properties, fatigue strength, fatigue crack propagation and microstructure. A feasibility study on the superplastic formability of the FG-STD butt joint was also conducted.

2. Experimental procedures

2.1. Laser beam welding

In this study, two different types of Ti-6Al-4V sheets, namely STD and FG sheets (with a 1.0-mm sheet thickness), were butt joined in a flat position by a continuous wave 3.3 kW Nd:YAG laser using Ti-6Al-4V filler wire (Grade 2, 1.0-mm diameter). The LBW process parameters were identified based on the previous experience of the Helmholtz-Zentrum Geesthacht (Torster et al., 1999). Table 1 shows typical LBW process parameters for the three welded specimens. The focal length was 200 mm, and the fibre diameter was 400 µm. The focus position F_{pos} = +2 mm refers to a focal plane position of 2 mm above the specimen surface. The welding direction was perpendicular to the rolling direction of the sheet

specimens, which were held fixed in an open box that was filled with Ar shielding gas to protect the weld bead from the ambient air during the LBW process. Fig. 1 shows the experimental set-up for the LBW of the Ti-6Al-4V sheets.

Table 1
LBW process parameters

Specimen No.	Power [kW]	F_{pos} [mm]	Welding Speed [m/s]	Wire Rate [m/s]
Specimen 1	1.8	0	0.05	0.05
Specimen 2	1.6	0	0.05	0.05
Specimen 3	1.6	+2	0.05	0.05

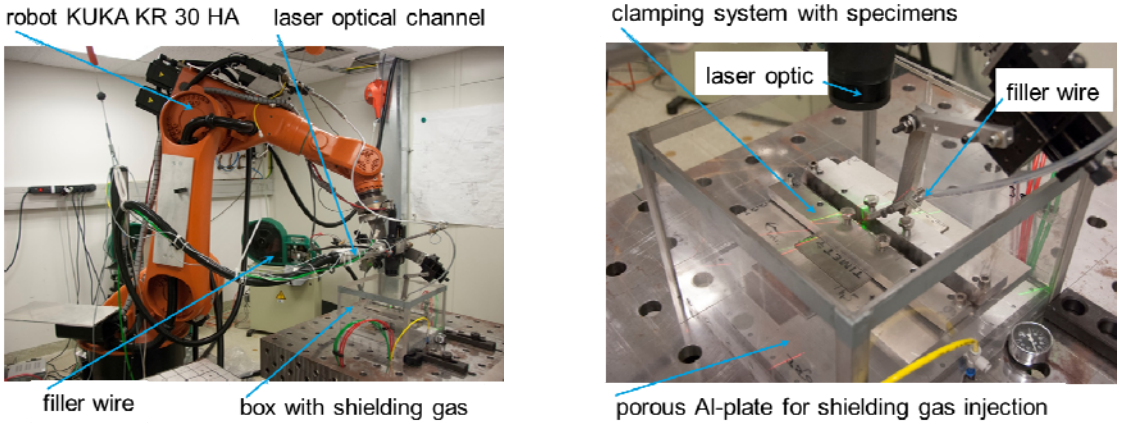

a) b)

Fig. 1 Experimental set-up for LBW of Ti-6Al-4V sheets

Fig. 2 shows the radiographs of the welded specimens using the parameters given in Table 1. The X-ray radiography was conducted according to DIN EN ISO 17636-1. Best results were obtained with the parameters used for specimen 3 (see Table 1 and Fig. 2(c)). Specimen 1 exhibited large underfilled areas, and the specimen 2 showed less underfills but some undercuts. The welding seam of specimen 3 had a regular shape in the longitudinal (L) direction. The welding seam of specimen 3 also did not exhibit cracks, pores, underfills or undercuts. Additional samples that were used for microstructural and mechanical characterisation and the cone-cup test were laser beam welded using the process parameters of specimen 3.

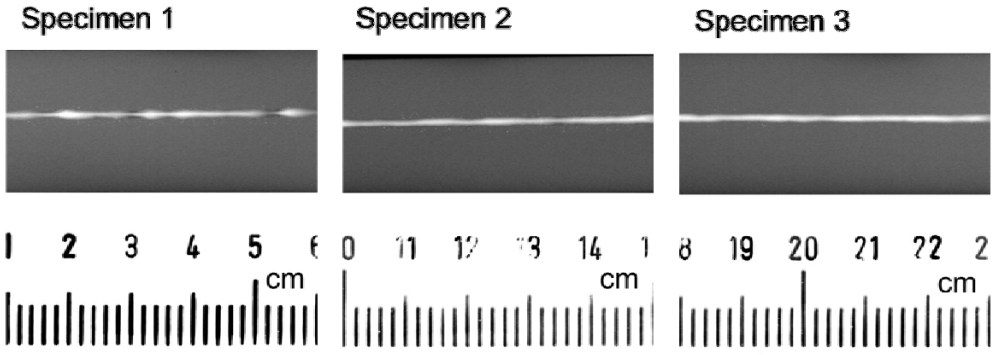

a) b) c)

Fig. 2 X-ray radiographs of specimens 1, 2 and 3 using the process parameters given in Table 1

2.2. Microstructural studies

The microstructure of the dissimilar laser beam welded Ti-6Al-4V FG-STD butt joints was studied using SEM with electron back-scatter diffraction (EBSD) to determine the local microtexture within the base material (BM), the heat-affected zone (HAZ) and the fusion zone (FZ), and the local chemical composition was determined using EDX. A metallographic specimen used for EBSD and EDX was ground and then electrolytically polished. The EBSD measurements were performed for a specimen area of 95 µm x 95 µm, at 25 kV, a spot size of 0.3 nA, an emission current of 75 µA, a magnification of 1000x, a working distance of 15 mm, a step size of 0.18 µm and a sample tilt of 70 °. The orientation calculation was based on the GSHE method, assuming a triclinic sample symmetry. The EDX analyses were performed at 15 kV, and the data obtained was calculated using the ZAF method. The microhardness profiles across the HAZ and FZ were obtained using an automated Vickers hardness testing machine with a 0.5-kg load.

2.3. Mechanical testing

Standard tensile tests at ambient temperature were performed according to DIN EN ISO 6892-1:2009. A 100-kN electro−mechanical universal testing machine (Schenck-Trebel RM100) was used to test the specimens at a constant traverse speed. The elongation of the samples was measured with a Fiedler Opto Electronics laser extensometer WS-160 with an initial length l_0 of 50 mm. For the welded specimens, the weld was always exactly in the middle of l_0.

A servohydraulic 25-kN machine with MTS electronics was used for the load-controlled fatigue tests at room temperature, a frequency of 40 Hz and a R-ratio of 0.1. Flat tensile specimens with a width of 20 mm and a parallel length of 60 mm were used. Two sets of each weld were tested: one set was as-welded, and the other set was completely milled to remove the undercut and surface notches in the weld zone. The run-out was defined as the point at which the specimen reached $10 \cdot 10^6$ cycles. For the fatigue crack propagation (FCP) tests, a 100-kN servo-hydraulic machine with MTS electronics was used. The tests were carried out in air. A constant load amplitude for a 10-Hz sinusoidal wave form was applied with a R-ratio of 0.1. The specimens were polished in the weld region to measure the crack length.

2.4. Cone-cup test

To determine the SPF behaviour of the tailored welded blanks, cone-cup tests were performed at FormTech. The cone-cup test was performed using a tool with a conical geometry. A blank was formed by applying gas pressure into this conical cavity at an approximately constant strain rate. The blank was clamped with a sufficiently high clamping force to prevent material flow into the flange region. Coaxial drawbeads were also used to prevent material flow and improve gas tightness. Details on the cone-cup test procedure and the test result analysis have been described by Beck, 2004.

The cone-cup tests were performed at 750 °C on an isothermal 100-metric-ton press. Argon gas was used to deform the blanks and as a shielding gas. Pressures of 0.92 MPa and 1.09 MPa were applied until the blanks fractured. The resulting dome height and the strain in the thickness direction were measured at the edge of the dome. The equivalent von Mises strain was calculated assuming constant volume.

3. Results and discussion

3.1 Microstructure and microhardness of laser beam welded Ti-6Al-4V joints

The chemical composition of Ti-6Al-4V controls the volume fraction of the hcp α and bcc β phases. The α phase has a higher strength and lower ductility than the β phase. Aluminium stabilises the α phase of titanium, and the β phase is stabilised by the addition of vanadium. EDX region analyses were conducted for the BMs and the FZ of the laser beam welded Ti-6Al-4V butt joint to determine the homogeneity of the chemical composition. The alloying elements shown in Table 2 were uniquely detectable by EDX. The Al content and V content of the FZ were found to be lower than those of the BMs. Differences of approximately 1.5 wt. % were observed for aluminium and of 0.5 wt. % - 1.0 wt. % for vanadium.

Table 2
Chemical composition of Ti-6Al-4V FG BM, the FZ of the FG-STD butt joint and Ti-6Al-4V STD BM obtained from EDX region analyses

Elements	**Ti-6Al-4V FG BM [wt. %]**	**Butt joint FZ [wt. %]**	**Ti-6Al-4V STD BM [wt. %]**
Al	6.84	5.44	6.98
Si	0.34	0.35	0.33
Ti	89.36	91.90	89.88
V	3.21	2.20	2.72
Fe	0.25	0.11	0.09

The mechanical behaviour of the rolled Ti-6Al-4V sheets is controlled by their grain size and texture. The Ti-6Al-4V FG sheet exhibited a fully equiaxed microstructure and contained 10.4 % the β phase. The average grain size was approximately 2.3 μm (see Fig. 3(a)-(b)). The single grain sizes were scattered over a region between 0.4 μm and 5.5 μm, whereas several grains exhibited larger sizes. The EBSD results showed that the Ti-6Al-4V FG sheet had a rotation texture, as can be observed by the orientation band in the (1 0 -1 0) pole figure in Fig. 3(c). The corresponding basal planes appear nearly parallel to the normal direction (ND) but are slightly tilted at a spread angle (see Fig. 3(c)). Thus, the texture components obtained from orientation density function (ODF) were near (1 1 -2 9)[-1 1 0 0] and (0 1 -1 5)[5 -5 0 1]. The prismatic (1 0 -1 0) planes in the transversal (T) direction exhibited a relatively high pole density. The β content of 11.2 % of the Ti-6Al-4V STD sheet was slightly higher than that for the FG sheet. The average grain size of the STD sheet was approximately 4.1 μm (see Fig. 4(a)-(b)).

The (0001) pole figure shows that a B/T texture is present in the Ti-6Al-4V STD sheet (see Fig. 4(c)).The direction of the basal planes was perpendicular to the T direction, as indicated by the maximum of the pole density. The single grain sizes of the equiaxed Ti-6Al-4V STD sheet ranged from 0.4 μm to 8.5 μm, and several larger grains could be observed.

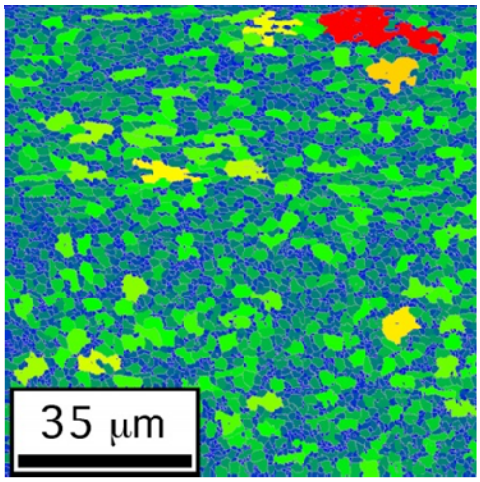

a)

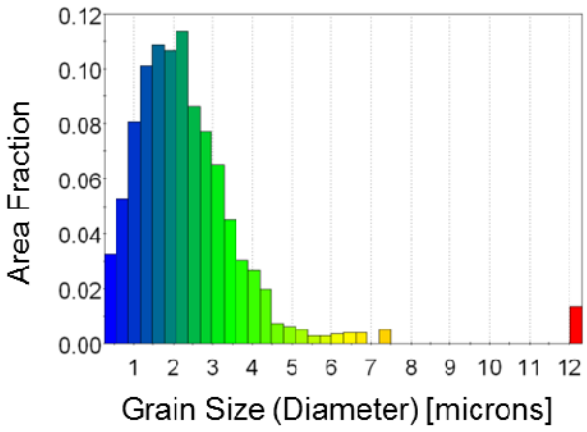

b)

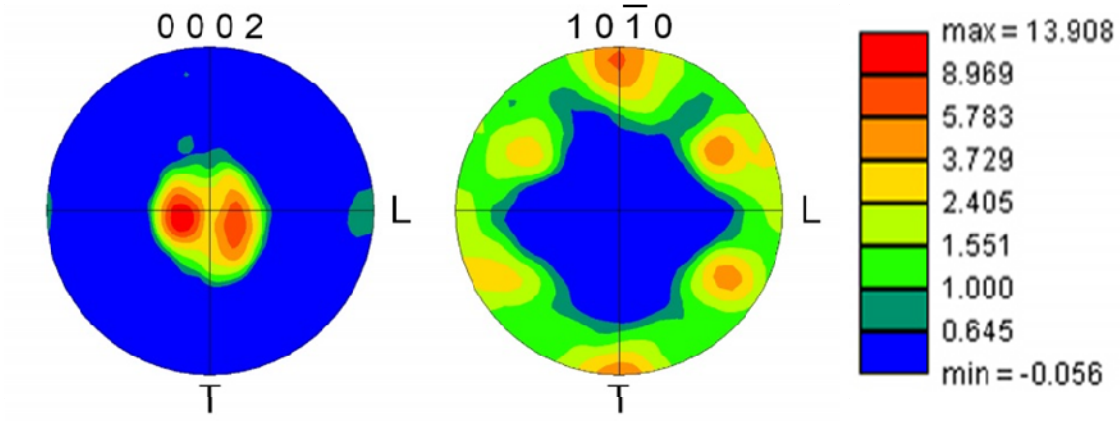

c)

Fig. 3 Ti-6Al-4V FG sheet, where L denotes the rolling direction and T denotes the transversal direction: the Ti-6Al-4V FG sheet contains 10.4 % the β phase, and the average grain size of the globular microstructure is approximately 2.3 μm (L_{max} = 22, P_{max} = 13.9 mrd)

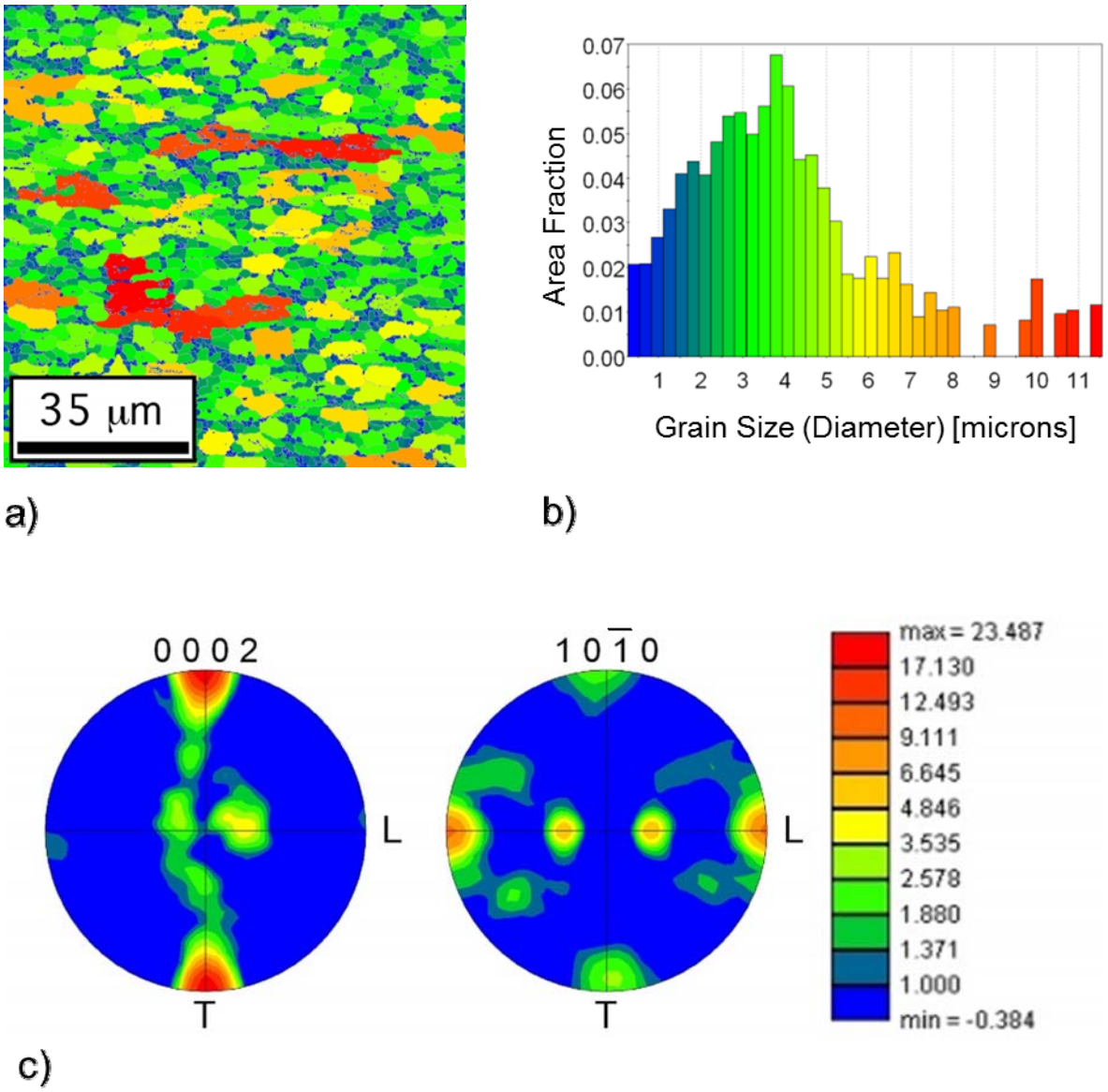

Fig. 4, Ti-6Al-4V STD sheet, containing 11.2 % the β phase: the average grain size in the globular microstructure is approximately 4.1 µm (L_{max} = 22, P_{max} = 23.5 mrd)

Pronounced basal textures, as in the Ti-6Al-4V STD sheet, lead to anisotropic material behaviour. For the direction independent comparison of the hardness, the Ti-6Al-4V STD sheet was turned 90° before LBW. So welding was transversal to the rolling direction for the Ti-6Al-4V FG sheet and parallel to the rolling direction for the STD sheet. Fig. 5 shows the cross-section of the laser beam welded butt joint with a symmetrical hourglass-shaped welding seam and the corresponding sample directions.

As previously mentioned, the BMs exhibited a fully equiaxed microstructure (see Fig. 6(a) and (e)). An orientation band from <1 0 -1 0>//T to <2 -1 -1 0>//T can be clearly seen in the S-L region of Ti-6Al-4V FG BM, whereas the pole density in the <2 -1 -1 0>//T crystal direction is comparatively low (see Fig. 6(a)). The S-L region of the Ti-6Al-4V STD BM exhibits a similar distribution with a maximal pole density in the <1 0 -1 0>//L crystal

direction and a low pole density in the <4 4 8 -5>//L crystal direction, indicating the presence of pyramidal planes (see Fig. 6(e)).

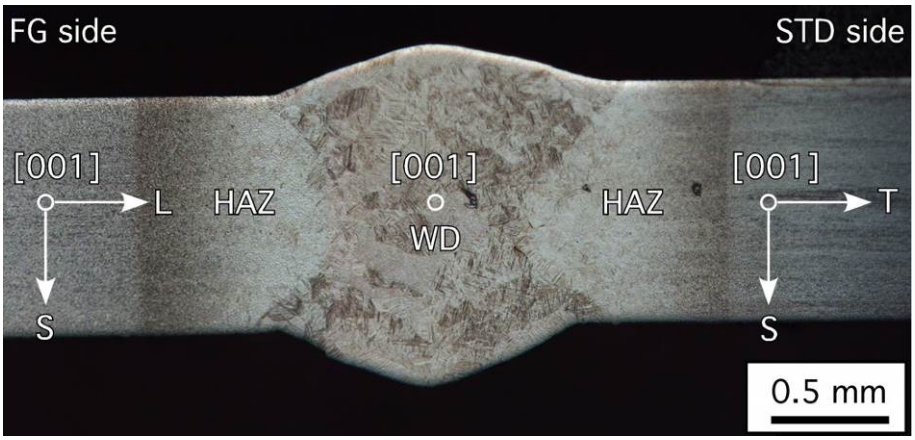

Fig. 5. Macrograph showing cross-section of the laser beam welded Ti-6Al-4V FG-STD butt joint (specimen 3, see Table 1): L, T, S and WD denote the longitudinal, transversal, thickness and welding directions, respectively

A significant change was observed for the HAZs adjacent to the FZ. Fig. 6(b) and (d) show that the equiaxed initial microstructure was transformed into an acicular morphology with embedded globular grains by the heat input during the LBW process and the subsequent cooling process. A phase analysis showed that the FG-sided HAZ region contained 13.7 % the β phase and that the STD-sided HAZ region contained 16.9 % the β phase. Orhan et al., 2001, reported that the amount of the β phase increased with the temperature and assigned the β-transition of the Ti-6Al-4V alloy to 995 °C. When the β content in the HAZs adjacent to the FZ was higher than that of the BMs, the temperature was assumed to be above the β temporary transus. Subsequent cooling from the β phase into (α+β)-phase activated the formation of acicular HAZ microstructures with a few embedded globular grains.

HAZ formation refined the grain size to approximately 1.8 µm and 1.9 µm. Distinct <0 0 0 1> crystal directions appeared within both HAZ regions, whereas the pole density of the <1 0 -1 0> crystal directions weakened relative to that of the BMs. Thus, the differences in the microstructural morphology and crystallographic orientation would have corresponded to metallurgical notches. It is well known that Ti-6Al-4V exhibits an intense sensitivity to notches, which is reflected in its mechanical behaviour under a cyclic load (Squillace et al., 2012).

The centre of the FZ consisted of colonies of martensitic plates with an average size of approximately 4.1 µm. Fig. 6(c) shows the martensitic microstructure, which consisted of 6.8 % the β phase and exhibited the following crystal directions: <1 2 -3 0>//WD, <1 1 -2 3>//WD, <0 2 -2 5>//WD and <0 2 -2 1>//WD. Thus, the fraction of the pyramidal crystal planes was higher than that of the BMs or the HAZs. A Ti-6Al-4V martensitic microstructure was formed by cooling along the reaction path $\beta \rightarrow (\alpha+\beta)$. If the cooling rate is higher than the critical cooling rate of 410 °C/s, a diffusionless transformation from the β phase to the α´ phase takes place (Squillace et al., 2012).

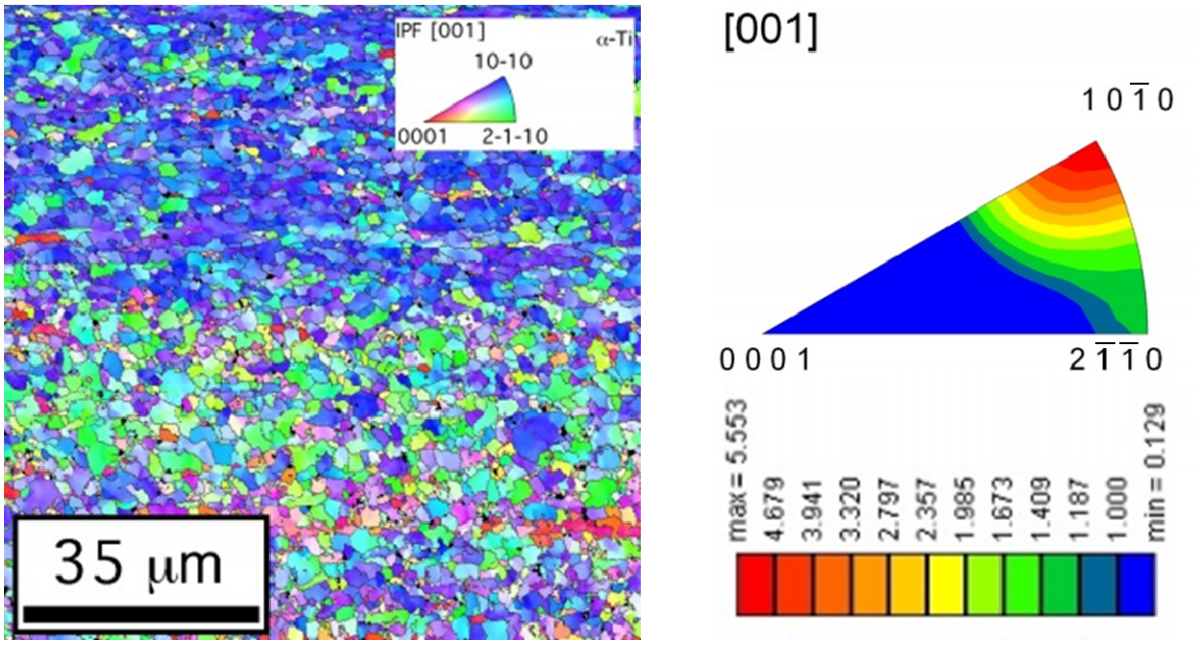
IPF [001]
α-Ti
10-10
0001
2-1-10
35 μm
[001]
1 0 $\bar{1}$ 0
0 0 0 1
2 $\bar{1}$ $\bar{1}$ 0
max = 5.553
4.679
3.941
3.320
2.797
2.357
1.985
1.673
1.409
1.187
1.000
min = 0.129

a)

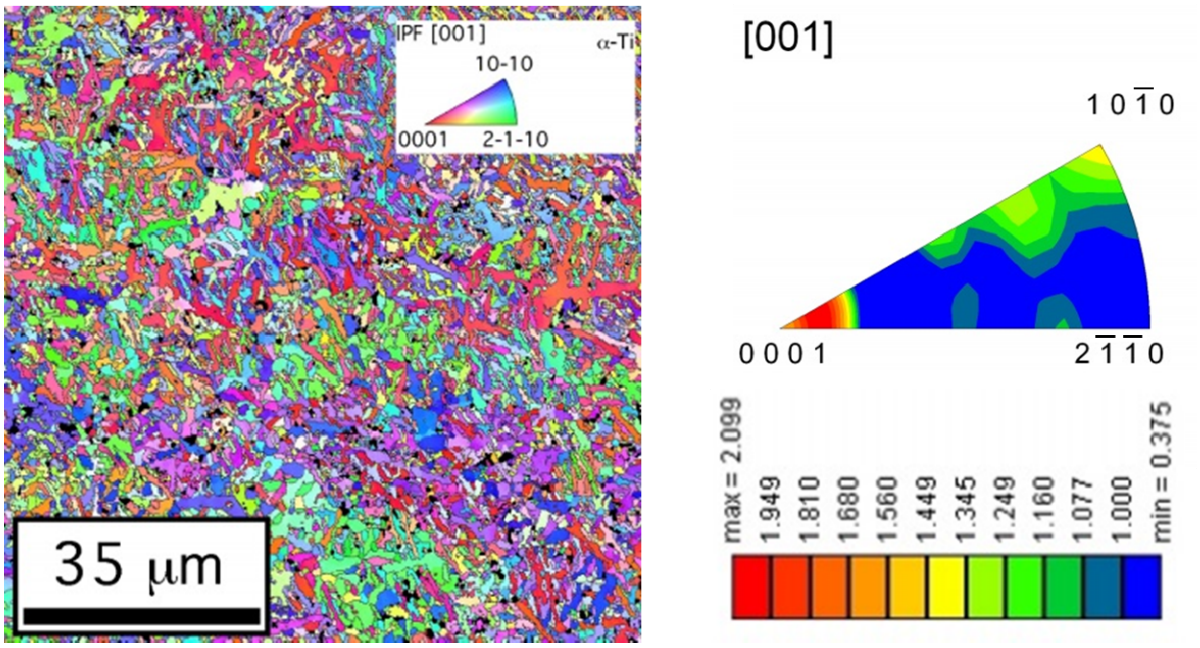
IPF [001]
α-Ti
10-10
0001
2-1-10
35 μm
[001]
1 0 $\bar{1}$ 0
0 0 0 1
2 $\bar{1}$ $\bar{1}$ 0
max = 2.099
1.949
1.810
1.680
1.560
1.449
1.345
1.249
1.160
1.077
1.000
min = 0.375

b)

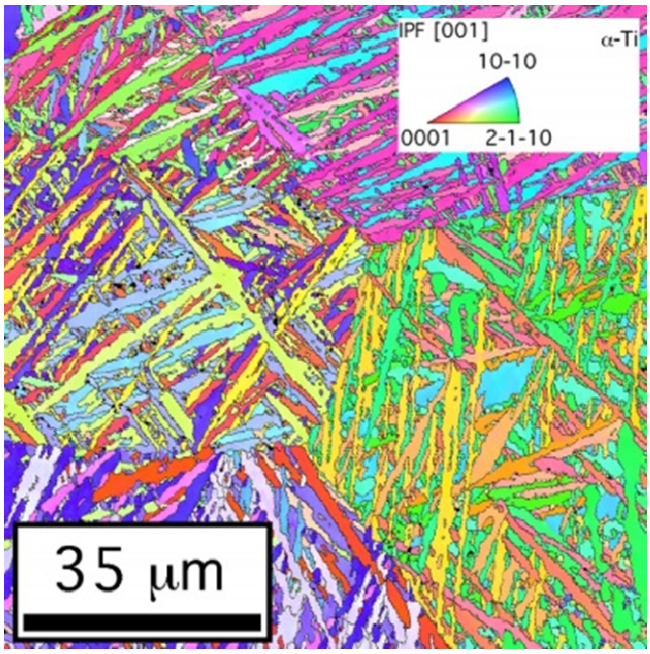
IPF [001]
α-Ti
10-10
0001
2-1-10
35 μm

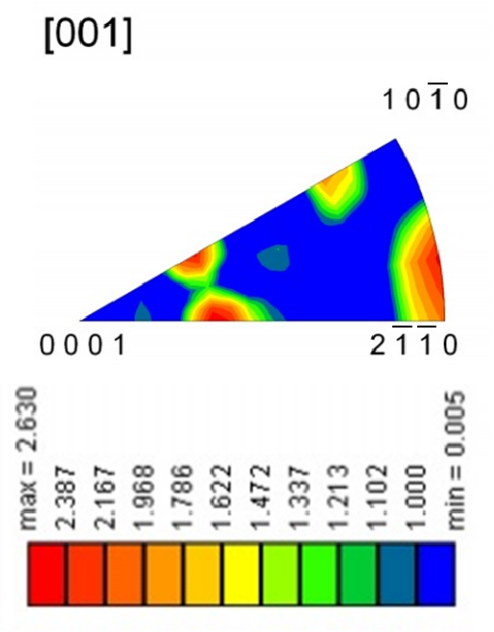
[001]
1 0 $\bar{1}$ 0
0 0 0 1
2 $\bar{1}$ $\bar{1}$ 0
max = 2.630
2.387
2.167
1.968
1.786
1.622
1.472
1.337
1.213
1.102
1.000
min = 0.005

c)

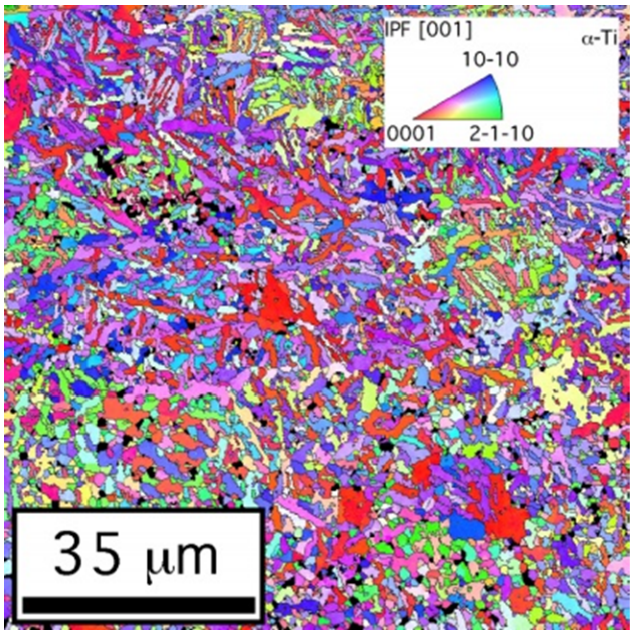
IPF [001]
α-Ti
10-10
0001
2-1-10
35 μm

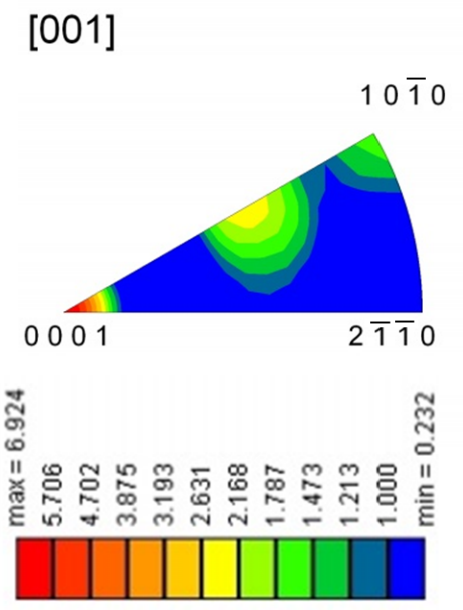
[001]
1 0 $\bar{1}$ 0
0 0 0 1
2 $\bar{1}$ $\bar{1}$ 0
max = 6.924
5.706
4.702
3.875
3.193
2.631
2.168
1.787
1.473
1.213
1.000
min = 0.232

d)

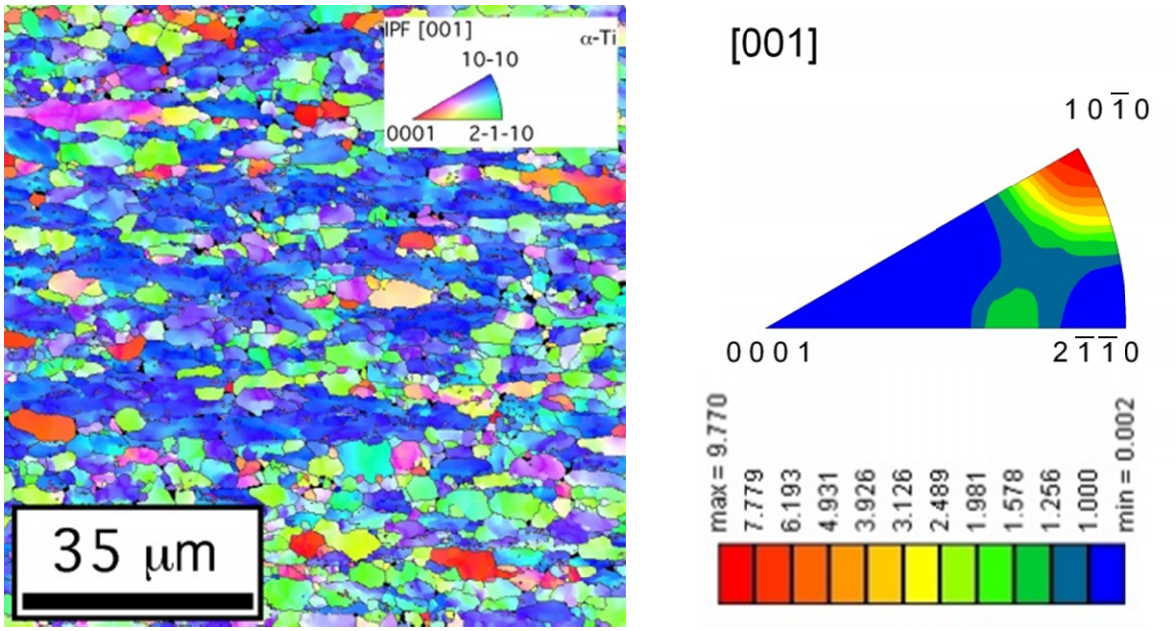

e)

Fig. 6. Orientation maps and inverse pole figures obtained from the middle region of the specimen cross-section: a) FG BM (L_{max} = 22, Pmax = 5.6 mrd), b) FG-sided HAZ (L_{max} = 22, Pmax = 2.1 mrd), c) FZ (L_{max} = 22, Pmax = 2.6 mrd), d) STD-sided HAZ (L_{max} = 22, Pmax = 6.9 mrd) and e) STD BM (L_{max} = 22, Pmax = 9.8 mrd); [001] is perpendicular to the specimen plane

The acicular microstructure inside the HAZs adjacent to the weld was formed because the cooling rate was sufficiently high enough to partially activate the diffusionless $\beta \rightarrow \alpha'$ transformation. The distance between the HAZs (shown in Fig. 6(b) and (d)) and the weld centre (shown in Fig. 6(c)) was approximately ± 1.0 mm. The HAZ close to each BM (where the distance to the weld centre of ±1.8 mm was used as a reference point) exhibited a fully equiaxed microstructure (see Fig. 6(a) and (b)).

Fig. 7 illustrates the importance of the texture on the behaviour of the yield stress as a function of the test direction, as described by Lütjering and Williams, 2003. When the test direction was perpendicular to the basal plane (at an angle of 0°), dislocations with the Burgers vector <a> could not be activated, because the Burgers vector <a> was parallel to the basal plane and the shear stress was zero. Dislocations with the Burgers vector <a+c> were allowed, and a much higher stress was required to activate their motion. The lowest value of the yield stress occurred at a 45° angle between the test direction and the basal planes where dislocations with the Burgers vector <a> could be activated more easily. At a 90° angle, the basal plane is parallel to the test direction. In this case, prismatic slip is possible and also requires a considerably high stress to occur (Lütjering and Williams, 2003).

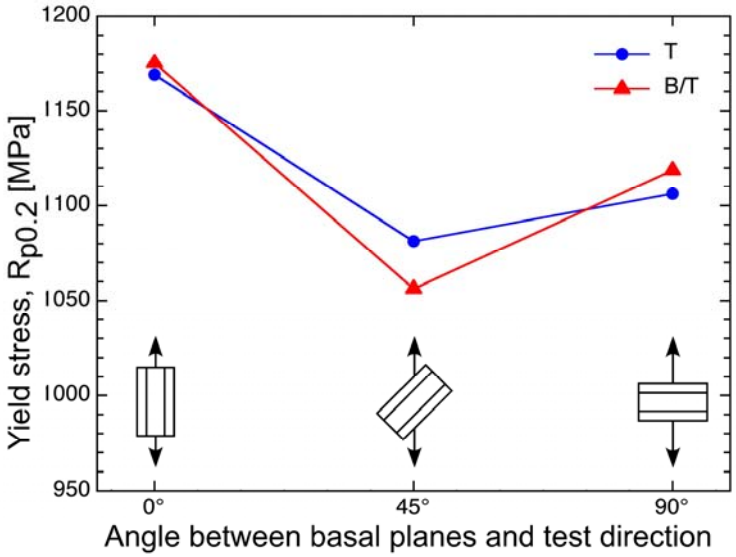

Fig. 7 Yield stress as function of the test direction, as determined from Ti-6Al-4V anisotropy (Lütjering and Williams, 2003)

Fig. 8 shows the hardness profiles that were determined across the weld in the middle region of the cross-section. The microhardness of the FG-BM was higher than that of the STD-BM. This response could be attributed to the different grain sizes, i.e., the Hall-Petch mechanism (Hall, 1951; Petch, 1953). The indentation was parallel to the <1 0 -1 0> crystal direction at ± 1.8 mm from the weld centre. The microhardness increased inside the HAZs from the BMs to the FZ because of the presence of the martensitic plates. The martensitic α´ structures in the Ti-6Al-4V alloy provide high strength and hardness accompanied by a loss of ductility and toughness. The contribution of the <0 0 0 1> crystal directions, which accumulated at a higher level in the HAZs, to the hardness could not be excluded.

In this study, the microhardness decreased at the transition from the HAZ to the martensitic FZ on both sides of the butt joint, as shown in Fig. 8. Studies on LBW of the Ti-6Al-4V alloy without filler wire showed that the lowest hardness values were found for the Ti-6Al-4V BM, and the highest hardness values were found for wedge-shaped welds (Squillace et al., 2012; Tsay and Tsay, 1997; Balasubramanian et al., 2011; Torster et al., 1999). Squillace et al., 2012, studied how the laser heat input affected the Ti-6Al-4V weld microhardness and found that the microhardness increased with the welding speed, which was controlled by increasing the cooling rate and by decreasing the heat input. On the basis of the arguments formulated by Squillace et al., 2012, it can be concluded that the cooling rate inside the FZ was lower than that in the nearby HAZ because of using a filler wire. The wire deployed extra molten material to the weld bead which acted via its mass as an external heat source. The orientation of the pyramidal crystal planes and the lower Al and V content did not play significant roles.

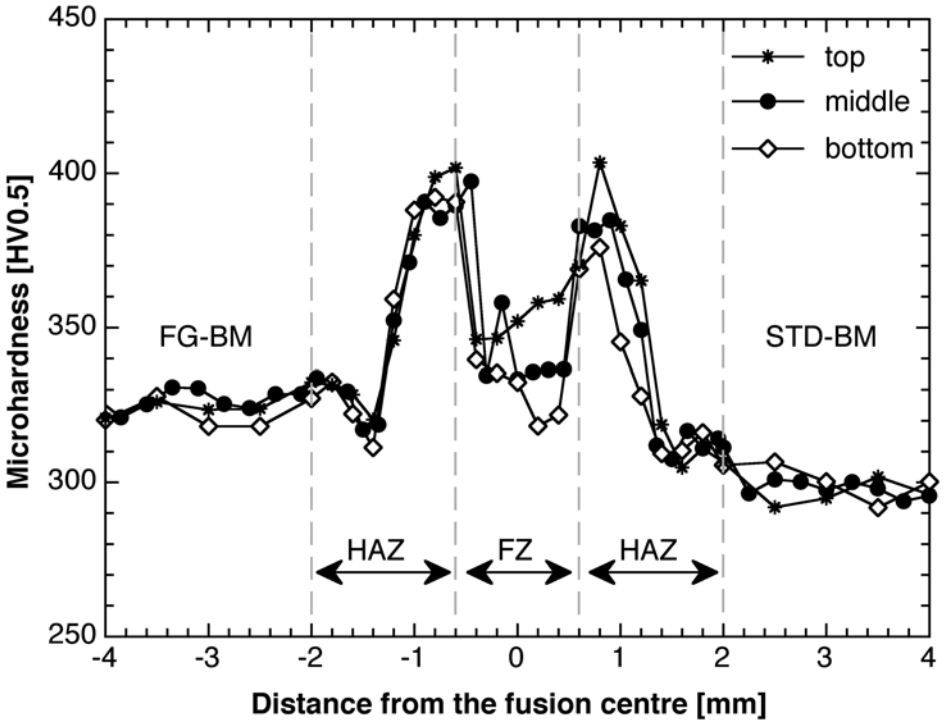

Fig. 8. Microhardness profiles of the dissimilar laser beam welded Ti-6Al-4V FG-STD butt joint of specimen 3 (see Table 1)

The average grain size of the martensitic HAZs was lower than that of the FZ (see Fig. 6(b)-(d)). Therefore, it can be assumed that the Hall-Petch mechanism was also active in the martensitic microstructures. Furthermore, comparing the aforementioned grain sizes confirmed that the cooling rates that produced the diffusionless $\beta \rightarrow \alpha'$ transformation in the HAZs and the welding seam were different.

3.3 Tensile tests

The behaviour of the Ti-6Al-4V STD and the Ti-6Al-4V FG sheets depends on the test direction because of the anisotropy of the hcp α phase. As previously mentioned, texture fundamentally affects the mechanical behaviour of the BM. Grain refinement increases the yield stress and the ultimate tensile strength. This effect results from the Hall-Petch mechanism (Hall, 1951; Petch, 1953). The laser beam welded Ti-6Al-4V FG-STD butt joint fractured inside the BM of the Ti-6Al-4V STD sheet. The condition of the HAZs, the laser beam weld and the Ti6-Al-4V FG BM did not affect the mechanical behaviour of the Ti-6Al-4V FG-STD butt joint under a static tensile load because their strengths were higher than that of the Ti-6Al-4V STD BM. The tensile data is summarised in Table 3, and the stress-strain curves are shown in Fig 9.

The effect of the strength mismatch was that the plastic deformation of the laser beam welded Ti-6Al-4V FG-STD butt joint was determined by the lower strength of the Ti-6Al-4V STD BM. Fig. 10 illustrates local differences in the response of the Ti-6Al-4V FG side, the welding seam and the Ti-6Al-4V STD side to the tensile load of the butt joint. These local differences were measured by applying four measurement marks on the specimen to divide it into three zones and the complete specimen. The distances between the marks were measured by a laser extensometer, and for each zone an independent data evaluation was made. Overall four tensile test results were gained from one specimen.

Table 3
Tensile strength of the Ti-6Al-4V STD sheet, the Ti-6Al-4V FG sheet and the dissimilar laser beam welded Ti-6Al-4V FG-STD butt joint. Average values with standard deviation of three tested specimens

Material / Direction	**$R_{p0.2}$ [MPa]**	**R_m [MPa]**	**A [%]**
Ti-6Al-4V STD BM			
L	959 ± 4.9	1016 ± 6	21 ± 2.1
T	986 ± 12	1036 ± 3	21 ± 1.4
Ti-6Al-4V FG BM			
L	1027± 2	1031 ± 8	12 ± 0.2
T	1065 ± 5	1061 ± 2	13 ± 0.9
LBW FG-STD	936 ± 3.1	1019 ± 1.3	8.5 ± 0.4

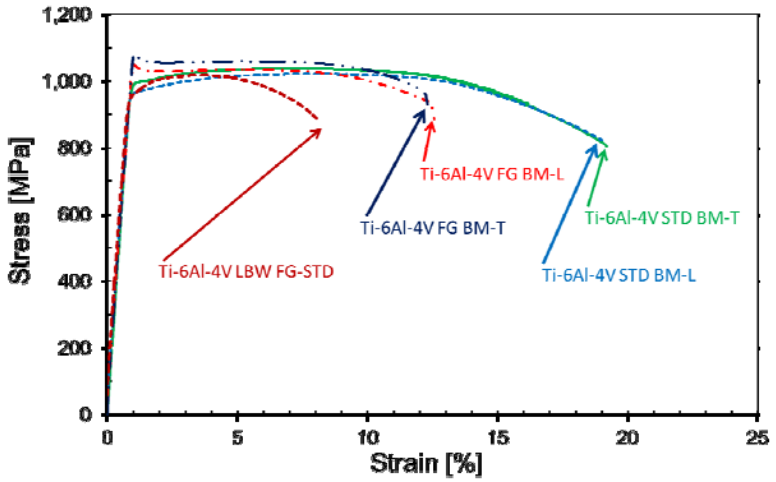

Fig. 9 Stress-strain curves of tested Ti-6Al-4V FG and STD BMs and dissimilar laser beam welded FG-STD butt joint

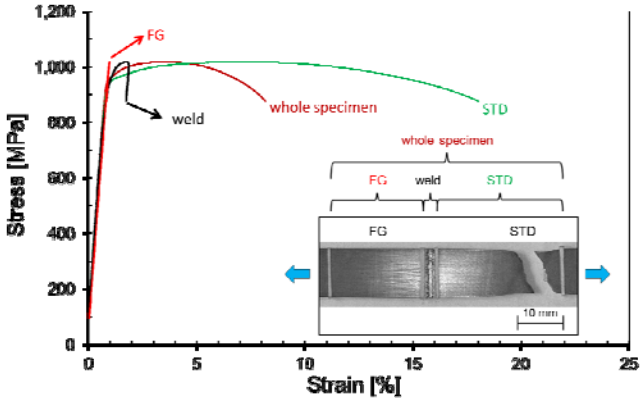

Fig. 10 Local differences in the mechanical behaviour of the FG BM, the STD BM and the laser beam weld

3.4 Fatigue and fatigue crack propagation tests

The fatigue strength has been correlated with the dependence of the yield stress on the grain size for equiaxed Ti-6Al-4V (Lütjering and Williams, 2003). The S-N curves shown in Fig. 11 confirm this trend, i.e., the fatigue limit of the Ti-6Al-4V FG sheet was higher than that of the Ti-6Al-4V STD sheet. Furthermore, the differences in the fatigue strength depended on the B/T texture of the Ti-6Al-4V STD sheet and the rotation texture of the Ti-6Al-4V FG sheet.

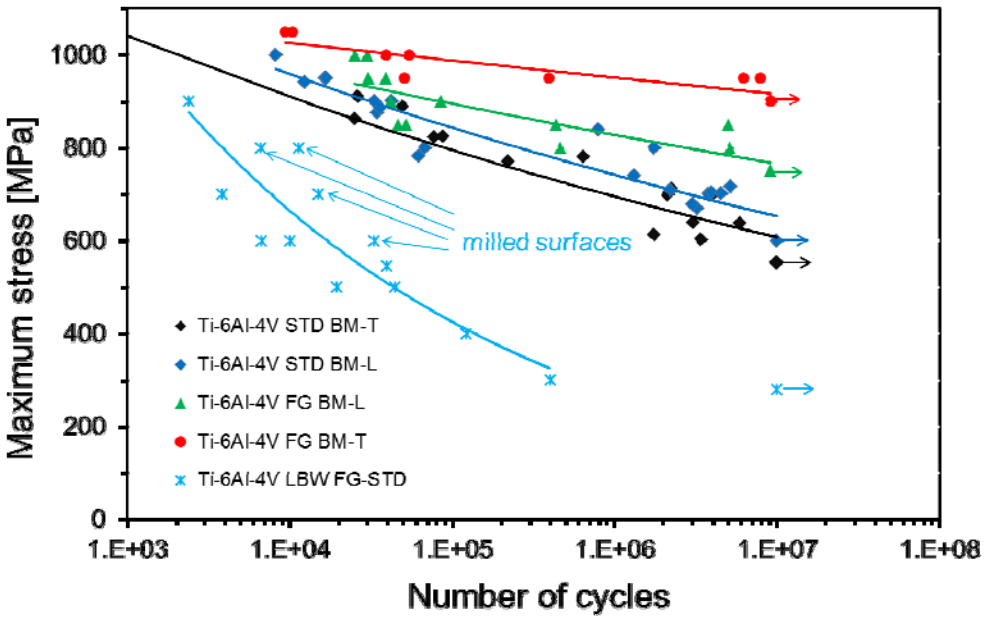

Fig. 11 S-N curves of Ti-6Al-4V FG sheet, Ti-6Al-4V STD sheet and laser beam welded FG-STD butt joint

Squillace et al., 2012, found that the fatigue life of a laser beam welded Ti-6Al-4V sheet without filler wire was strongly affected by the value of the underfill radius, whereas the S–N curve tended to move towards regions of higher cycles as the underfill radius in the laser weld increased. These results confirmed the notch sensitivity of the laser beam welded Ti-6Al-4V alloy. However, the filler wire that produced the overfilling of the symmetrical hourglass-shaped welding seam did not extend fatigue life. Moreover, removing the weld surface and weld root of the specimens did not significantly improve the fatigue behaviour of these specimens. This result may be attributed to the presence of metallurgical notches produced by local changes in the microstructure and the microtexture during LBW. The fracture failure of the welded specimens always occurred in the STD-sided HAZ adjacent to the solidification line (see Fig. 12).

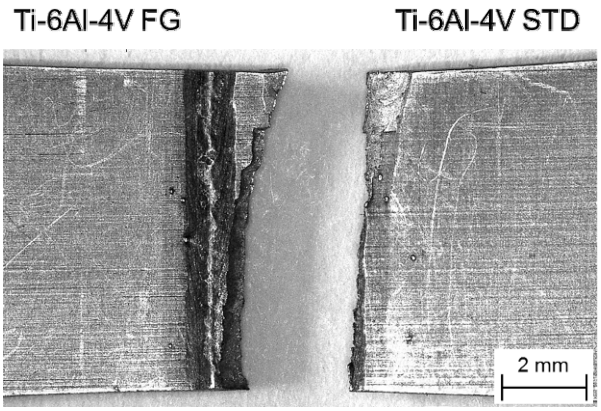

Fig. 12 Interface failure between welding seam and HAZ

Wagner and Gregory, 2003, found that short fatigue cracks propagated faster in coarse-grained titanium than in fine-grained titanium for reported grain sizes of 20 µm and 100 µm, respectively, and equal values of the stress intensity factor ΔK. Fine-grained titanium has a higher grain boundary density, which increases the resistance to FCP, because grain boundaries are effective obstacles to crack motion. The opposite behaviour was observed for long cracks in coarse-gained titanium because of deviations from ideal crack front geometry and crack closure. However, the increase in the grain size from 2 µm to 12 µm only produced slight changes in the FCP rates for equiaxed Ti-6Al-4V (Wagner and Gregory, 2003). The da/dN-ΔK curves in Fig. 13 show that the difference between the grain sizes of 2.3 µm and 4.1 µm for the Ti-6Al-4V FG sheet and the Ti-6Al-4V STD sheet, respectively, was not sufficiently large to significantly affect FCP. This result is in good agreement with the results of Wagner and Gregory, 2003. The Ti-6Al-4V FG sheets exhibited a shorter life in the L direction than in the T direction, which was attributed to their texture, i.e., FCP was slower in the T direction than the L direction (see Fig. 13).

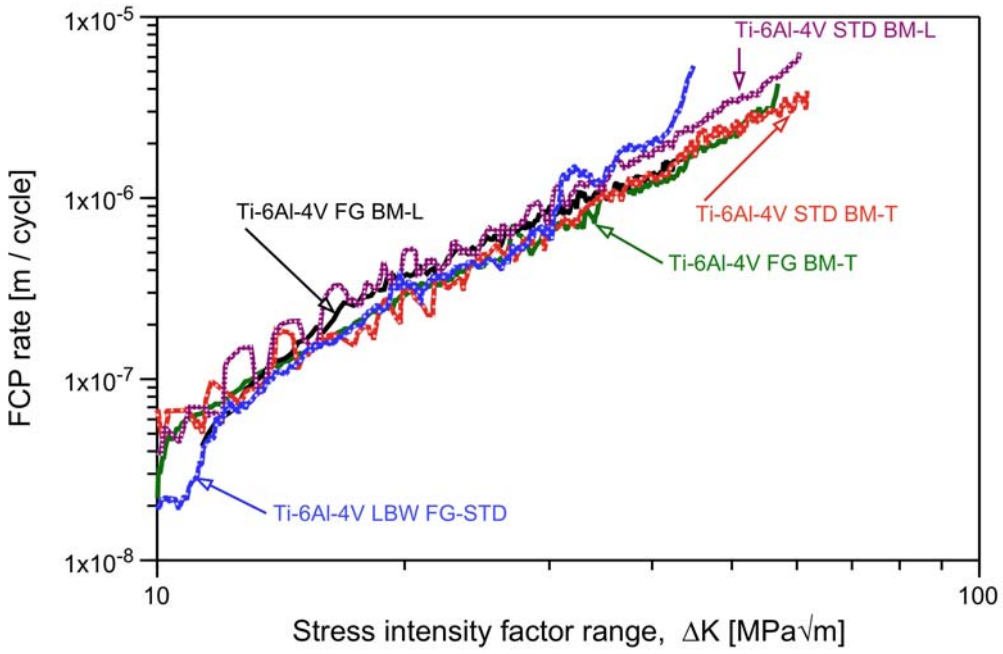

Fig. 13 FCP test results

At lower values of the stress intensity factor ΔK, the welding seam exhibited significantly lower FCP rates than those of the BMs. The martensitic FZ and its less sharp texture relative to that of the BMs resulted in a more pronounced deviation of the crack path. As the stress intensity factor ΔK increases, the da/dN-ΔK curves for the laser beam welded butt joint were quite similar to those of the Ti-6Al-4V STD sheet and the Ti-6Al-4V FG sheet in the mid-regime (Paris regime) (see Fig. 13). The fatigue crack in the laser beam welded butt joint specimen deviated away from the weld into the STD-sided HAZ at $\Delta K \approx 30$ MPa$\sqrt{m}$. This result showed that the FCP properties of the welding seam were superior to those of the HAZs. Similar observations were obtained by Li et al., 2011, for EBW and by Tsay and Tsay, 1997, for LBW. The FCP behaviour of the BMs is nearly identical for similar directions.

For EBW, heterogeneity in the weld seam greatly affected the FCP. The FCP through or along the primary alpha grain in the HAZ exhibited few deflections and branching. Therefore, the HAZ had less FCP resistance than the FZ because of the effects of heterogeneity. Keshava Murthy and Sundaresan, 1997, also found that the FCP resistance of the welded material increased significantly for EBW and TIG, which was attributed to the improvement in the FCP behaviour because of the lamellar microstructure in the FZ and to the tensile residual stresses normal to the fatigue load. For cast Ti-6Al-4V, the inferior FCP behaviour of the welded material (by EBW and TIG) was compared to that of the BM (Oh et al., 2003). Balasubramanian et al., 2011, reported inferior FCP behaviour for welded specimens.

3.5 Cone-cup tests

The results of the cone-cup tests on the welded blanks at 750 °C are shown in Fig. 14 and Table 4. Fig. 14 shows the deformed cones after fracture. The cone consisted of a conical section and a hemispherical section at the top, which is referred to as a dome. The crack occurred in the dome region. The weld deformed along with the surrounding material, and neither the weld nor the HAZ served as a crack initiation site. Note that the weld, albeit originally in the centre of the blank, was not centred on the dome peak. Instead, the weld shifted, and the complete dome consisted of FG material. The FG material obviously deformed preferentially under a constant applied gas pressure. Thus, the FG material exhibited a lower flow stress at 750 °C than that of a conventional STD material. At elevated temperatures and low strain rates, deformation mechanisms, such as grain boundary sliding, can contribute to the overall deformation. A small grain size promotes grain boundary sliding. Thus, a reduction in the grain size could be correlated with the reduction in the flow stress at 750 °C.

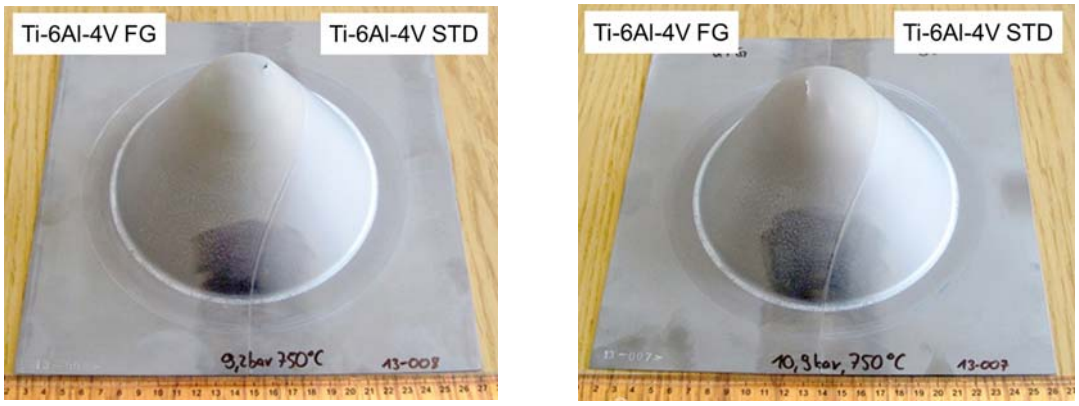

a) b)

Fig. 14 Deformed specimens from the cone-cup test a) at 0.92 MPa and b) 1.09 MPa

Table 4 shows the thickness reduction, which was measured after the test at the dome edge, along with the dome height and the calculated average strain rate of the cone-cup test. The dome edge was assumed to deform stably without necking. Thus, the reduction in the thickness at the dome edge can be considered to be a limit strain for safe forming of components. Under the assumption of constant volume and biaxial strain, the von Mises strain was found to be the absolute value of the measured thickness reduction.

Table 4
Cone-cup test results

Pressure [MPa]	**Dome height [mm]**	**Thickness reduction [-]**	**Von Mises strain [-]**	**Average strain rate [s^{-1}]**
0.92	102	-1.7	1.7	$1.1x10^{-3}$
1.02	96	-1.4		$1.5x10^{-3}$

Comparing the cone-cup test results at 0.92 MPa and 1.02 MPa showed that the slight increase in the pressure of 0.1 MPa had a significant effect on the SPF behaviour. The resulting von Mises strain at the dome edge increased by 0.3. At the same time, the time to fracture decreased from 25 to 16 minutes, and the average strain rate increased by $0.4x10^{-3}$ s^{-1}. Thus, increasing the pressure can reduce the cycle time for industrial SPF processes, whereas decreasing the pressure can increase the formability at elevated temperatures.

A strain rate in the order of magnitude of $1x10^{-3}$ can be considered to be suitable for industrial SPF processes. While common titanium alloy sheets exhibit SPF behaviour at either higher temperatures or significantly lower strain rates, the FG material is deemed a promising candidate to realise a higher productivity of SPF processes.

It is especially notable that the weld deformed along with the BMs and was not the crack initiation site. The conducted cone-cup tests proved the feasibility of SPF of a welded blank with a dissimilar joint. The achieved degree of deformation can be considered to be sufficient for aerospace applications and was not limited by the mechanical properties of the weld or the HAZ. The use of tailored blanks with dissimilar joints can improve the spectrum of applications for SPF of titanium alloy sheets.

4. Conclusions

- The microstructural and mechanical properties of 1.0-mm thick dissimilar laser beam welded Ti-6Al-4V sheets were investigated for different grain sizes and conditions. A Ti-6Al-4V FG sheet that has been developed for SPF processes at temperatures under 950 °C was successfully joined to an aircraft-approved Ti-6Al-4V STD sheet without welding defects using a Nd:YAG laser.

- A symmetrically overfilled hourglass-shaped welding seam without cracks, pores or undercuts was produced. The butt joint consisted of a martensitic FZ, inhomogeneous HAZs and equiaxed BMs.

- The HAZs exhibited a martensitic microstructure adjacent to the FZ and an equiaxed microstructure adjacent to the BMs. The local microstructure transformations were associated with changes in the microtexture and the grain size and an increase in the

hardness. The hardness decreased at the transition from the HAZs to the martensitic FZ zone on both sides of the butt joint because of the use of alloy-compatible filler wire. The presence of microstructural and crystallographic heterogeneities was considered to act as a metallurgical notch.

- The mismatch in the strength from the increase in the hardness resulted in the plastic deformation of the dissimilar laser beam welded butt joint, which was determined by the lower strength and higher ductility of the Ti-6Al-4V STD sheet. The fracture failure of the butt joint under a static tensile load occurred in the BM.

- The fatigue strength was correlated with the dependence of the yield stress on the grain size for equiaxed Ti-6Al-4V sheets and was also related to the B/T texture of the Ti-6Al-4V STD sheet and the rotation texture of the Ti-6Al-4V FG sheet. The laser beam welded butt joint exhibited inferior fatigue properties compared to the BMs because of the geometrical notch effect of the welding seam. The fatigue fracture occurred at the interface between the HAZs and the FZ. Removing the weld surface and the weld root to reduce surface roughness did not significantly improve fatigue behaviour, i.e., the metallurgical notch also resulted in fracture at the interface between the HAZs and the FZ.

- The FCP behaviour of the laser beam welded FG-STD butt joint was at least comparable to that of the BM sheets. The T-direction of both sheets exhibited slightly lower FCP rates than the L-direction.

- SPF displaced and bent the welding seam from its original position at the centre to the cone-cup surface without forming cracks in the HAZs or the FZ. The deformation primarily occurred in the Ti-6Al-4V FG sheet. The welding seam of the dissimilar FG-STD Ti-6Al-4V butt joint was resistant to SPF.

Acknowledgements

This work was carried out under the auspices of the CoolTiTech project, which was funded by the German Federal Ministry of Economics and Technology (BMWi) under the LuFo IV-3 program. The financial support of the German BMWi is gratefully acknowledged. The authors also thank the following project members for their valuable work and support: Mr. K. Erdmann (mechanical testing), Mr. P. Haack (X-ray testing), Mr. R. Dinse (LBW), Mr. F. Dorn (metallography/EBSD), and Mr. L. Bieneck (cone-cup tests).

References

Balasubramanian, T.S., Balakrishnan, M., Balasubramanian, V., Muthu Manickam, M.A., 2011. Influence of welding processes on microstructure, tensile and impact properties of Ti-6Al-4V alloy joints. Transactions of Nonferrous Metals Society of China. 21, pp. 1253-1263.

Balasubramanian, T.S., Balasubramanian, V., Muthu Manickam M.A., 2011. Fatigue crack growth behaviour of gas tungsten arc, electron beam and laser beam welded Ti-6Al-4V alloy. Materials and Design. 32, pp. 4509-4521.

Beck, W., 2002. Superplastic forming and diffusion bonding of titanium and titanium alloys in German. In: Peters, M., Lyens, C. (Eds.), Titan und Titanlegierungen, 3rd. ed. Hardcover: Wiley-VCH, Weinheim, Germany, pp. 285-301.

Beck, W., 2004. Results of in-house cone-cup testing of low to high temperature SPF-alloys. Materials Science Forum 447-448, pp. 145-152. doi:10.4028/www.scientific.net/MSF.447-448.145

Cao, X., Jahazi, M., 2009. Effect of welding speed on butt joint quality of Ti-6Al-4V alloy welded using a high-power Nd:YAG laser. Optics and Lasers in Engineering. 47, pp. 1231-1242.

Hall, E.O., 1951. The deformation and ageing of mild steel: III discussion of results. Proc. Phys. Soc. 64, pp. 747-753.

Hanse-Aerospace e.V., 2012. Tie rods aus Titan Ti6-4 für A350. Hanse-Aerospace Bulletin 02, pp. 8-8. Available from http://www.hanse-aerospace.net/uploads/media/bulletin-02-2012-web.pdf

Hombergsmeier, E., 2010. Hybrider Leichtbau im Flugzeugbau von Glare® bis HTCL. Hybridica forum, 2010 Nov 9, Munich, Germany. Available from http://media.nmm.de/62/hybridicahombergsmeierhandout_24446062.pdf#

Jianxun, Zh., Xu, S., Li, Zh., 2012. Investigation into plastic damage behaviour of the CO_2 laser deep penetration welded joint for Ti-6Al-4V alloy. Engineering Fracture Mechanics. 83; pp. 1-7.

Keshava Murthy, K., Sundaresan, S., 1997. Fatigue crack growth behaviour in a welded α-β Ti-Al-Mn alloy in relation to microstructure features. Materials Science and Engineering A. A222, pp. 201-12.

Li, X., Hu, Sh., Xiao, J., Ji, L., 2011. Effects of the heterogeneity in the electron beam welded joint on fatigue crack growth in Ti-6Al-4V alloy. Materials Science and Engineering A. 529, pp. 170-177.

Lütjering, G., Williams, J.C., 2003. Titanium, Springer-Verlag Berlin, Heidelberg.

Murakami. S., Ozaki, K., Ono, K., Itsumi, Y., 2011. Effect of alloying on machinability and hot workability of α-β titanium alloy containing Fe and C. 13 Kobelco Technology Review. 20, pp. 1-18. Available from http://www.kobelco.co.jp/english/ktr/pdf/ktr_30/013-018.pdf

Oh, J., Kim, N.J., Lee, S., Lee, E.W., 2003. Correlation of fatigue properties and microstructure in investment cast Ti-6Al-4V welds. Materials Science and Engineering A. A340, pp. 232-233.

Orhan, N., Khan, T.I., Eroglu, M., 2001. Diffusion bonding of a microduplex stainless steel to Ti-6Al-4V. Scripta Materialia. 45-4, pp. 441-446.

Pei-quan, X.U., 2012. Microstructure characterization of Ti-6Al-4V titanium laser weld and its deformation. Transactions of Nonferrous Metals Society of China. 22, pp. 2118-2124.

Petch, N.J., 1953. The cleavage strength of polycrystals. J. Iron Steel Inst. 174, pp. 25-33.

Peters, M., Hemptenmacher, J., Kumpfert, J. and Leyens, C., 2002. Titanium and titanium alloys: structure, microstructure and properties in German. In: Peters, M., Lyens, C. (Eds.), Titan und Titanlegierungen, 3rd. ed. Hardcover: Wiley-VCH, Weinheim, Germany, pp. 1-36.

Petersen. M., 2012. Process development and mechanical performance of 4mm Ti-6Al-4V laser-GMAW hybrid welds. Presented at TWI/EWI Aerospace Joining Seminar; 2012 Sep 13, Munich, Germany.

Rai, R., Elmel, J.W., Palmer, T.A., DebRoy, T., 2007. Heat transfer and fluid flow during keyhole mode laser welding of tantalum, Ti-6Al-4V, 304L stainless steel and vanadium. J. Phys. D: appl. Phys. 40, pp. 5753-5766. Online at stacks.iop.org/JPhysD/40/5753

Rosell, A., 2013. System for lifetime assessment of laser-welded titanium component. Presented at 4th CEAS Air and Space Conference, 2013 Sep 16-19 Linköping, Sweden.

Salishchev, G.A., Valiakhmetov, O.R., Galeyev, R.M., Froes, F.H., 2004 Characterization of submicron-grained Ti-6Al-4V sheets with enhanced superplastic properties. Materials Science Forum. 447-448, pp. 441-446.

Saresh, N., Gopalakrishna Pillai, M., Mathew, J., 2007. Investigation into effects of electron beam welding on thick Ti-6Al-4V titanium alloy. Journal of Materials Processing Technology. 192-193, pp. 83-89.

Squillace, A., Prisco, U., Ciliberto, S., Astarita, A., 2012. Effect of welding parameters on morphology and mechanical properties of Ti-6Al-4V laser beam welded butt joints. Journal of Materials Processing Technology. 212, pp. 427-437.

TITAL, 2013. TITAL benefits from composite-trend. Information on http://www.tital.de/it/news/attualit/tital-benefits-from-composite-trend.html

Torster, F., dos Santos, J.F., Kocak, M., Penasa, M., 1999. Mechanical and microstructural characterization of laser beam welded titanium alloys. In: Proceedings of the 5th International Conference on Trends in Welding Research, ASM International, Materials Park, Ohio, USA, pp. 887-892.

Tsay, L.W. and Tsay, C.Y., 1997. The effect of microstructure on the fatigue crack growth in Ti-6Al-4V laser welds. International Journal of Fatigue. 19(10), pp. 713-721.

Vallhagen, J., 2013. Robust design and DFM-methodology for aerospace engine components. Presented at 4th CEAS Air and Space Conference, 2013 Sep 16-19 Linköping, Sweden.

VSMPO Avisma, 2013. Information from http://www.vsmpo.ru/ru/

Wagner, L., Gregory, J.K., 2003. Fatigue of titanium alloys in German. In: Peters, M., Lyens, C. (Eds.), Titan und Titanlegierungen, 3rd. ed. Hardcover: Wiley-VCH, Weinheim, Germany, pp. 163-194.

Wang, S., Wu, X., 2012. Investigation on the microstructure and mechanical properties of Ti-6Al-4V alloy joints with electron beam welding. Materials and Design. 36, pp. 663-671.

Wang, S.H., Wie, M.D., Tsay, L.W., 2003. Tensile properties of LBW welds in Ti-6Al-4V alloy at evaluated temperatures below 450°C. Materials Letters. 57, pp. 1815-1824.

Wanjara, P., Brochu, M., Jahazi, M., 2005. Ti-6Al-4V electron beam weld qualification using laser scanning confocal microscopy. Materials Characterization. 54, pp. 254-263.